Article

Facile Seed-Mediated Growth of Ultrathin AuCu Shells on Pd Nanocubes and Their Enhanced Nitrophenol Degradation Reactions

Siva Kumar Krishnan,* Rodrigo Esparza, Daniel Bahena Uribe, Sundeep Mukherjee, and Umapada Pal*

Read Online

ACCESS | Metrics & More | Article Recommendations | SI Supporting Information

ABSTRACT: Multimetallic core−shell nanocrystals (NCs) with precise control over shell thickness down to few atomic layers have attracted tremendous interest for a variety of catalytic reactions. However, limitations associated with large lattice mismatch, particularly for the metals with a larger lattice mismatch, remained a great challenge in generating multimetallic core−shell NCs. Herein, we demonstrate seed-mediated coreduction of AuCu onto Pd nanocube seeds to obtain Pd@AuCu$_{nL}$ (n = 6,12) core−shell nanocubes with atomic-level control over shell thickness and near-perfect lattice matching of the core−shell interface. Precise control over the shell layer thickness from six to twelve atomic layers could be possible by slow and simultaneous codeposition of the Au and Cu precursors, i.e., $AuCl_2(OH)_2^-$ and $Cu(OH)_2^-$ ions, by controlling the OH^- ion concentration (i.e., pH) in the reaction solution with a low Cu content. Moreover, Pd@AuCu$_{nL}$ core−shell NCs with different shapes such as hexagonal and concave NCs were readily obtained by modulating the reduction kinetics of metal precursors in seeded growth. Importantly, obtained Pd@AuCu$_{6L}$ core−shell nanocubes manifested best catalytic performance for the reduction of 4-nitrophenol (4-NP) by NaBH$_4$. The high catalytic activity of the core−shell nanocubes has been ascribed to the synergetic effect of the Pd core and the AuCu alloy shell. The simple, solution-based approach utilized in this work can be adapted for controlled synthesis of other multimetallic core−shell nanocubes with atomically controlled shell thickness for a variety of heterogeneous catalysis reactions.
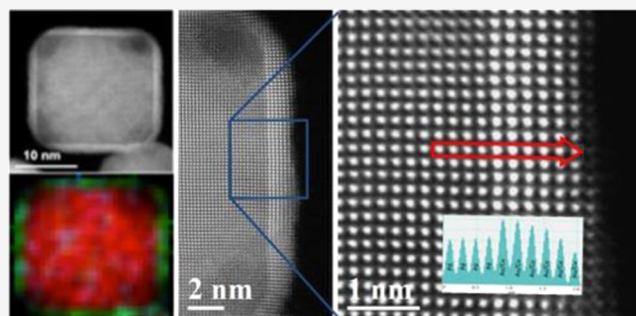
1. INTRODUCTION

Multimetallic nanocrystals (NCs) of tailored composition, structure, and geometry have attracted tremendous attention due to their tunable functionalities and a range of potential applications in fields such as in catalysis,[1] photocatalysis,[2] biomedicine,[3] and biosensing.[4] Apart from size and shape, the possibility of composition manipulation offers an additional opportunity to tune the catalytic performance of multimetallic NCs, which is difficult to attain in their monometallic counterparts.[5,6] On the other hand, bi/multimetallic core−shell NCs consisting of a few atomic-layer-thick shells onto other metallic substrates have received huge attention for a variety of catalytic reactions due to outstanding catalytic performance and reduced consumption of precious metals.[7−10] The extraordinary catalytic activity of these core−shell NCs could be attributed to the synergetic effects of geometry and electronic features originating from their core and shell interface.[11] It is well accepted that reducing the shell thickness to a few atomic layers increases the lattice strain and electronic effects on the outer surface of core−shell NCs, which significantly maximize the catalytic performance.[9,12−14] Among the multimetallic NCs, deposition of few atomic-layer-thick noble metals such as gold−copper (Au−Cu) on Pd nanocubes is highly desired because it can provide functional catalytic sites on the surface of the NCs and enhance their

catalytic activity.[15] In fact, the noble metal nanoparticles such as Ag, Au, and Cu have been demonstrated to cover Pd NCs to produce Pd@M (M = Ag, Au, Cu) core−shell-type NCs and shown to exhibit superior catalytic performance.[16−20] While the integration of plasmonic bimetallic shells such as AuCu over nonplasmonic Pd NCs creates significant surface strain because of large lattice mismatch of the elements, it alters the electronic structure of the multimetallic system, boosting their catalytic performace.[12,14,20]

Seed-mediated solution-phase methods have been utilized frequently for the synthesis of bimetallic and multimetallic core−shell NCs, in which precursors of metallic shells are deposited over a presynthesized metallic core (seed substrate) at a relatively slower rate utilizing a mild reducing agent.[21−23] Uniform deposition of a shell layer over a seed substrate is largely governed by the reduction kinetics of metal ions, their reduction and diffusion rates,[24,25] and lattice mismatch of the
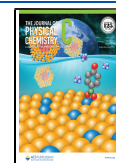
metals.[26] Although significant progress has been made on kinetically controlled synthesis of bi/multimetallic core−shell NCs with distinct shapes,[23,24,27] obtaining bimetallic alloy shells with precise control over thickness remained a great challenge, particularly for the metals with a larger lattice mismatch.[28,29] It was demonstrated that monometallic Au and Ag shells could be easily grown over Pd nanocubes by controlling the reduction kinetics of corresponding ions.[30] However, uniform codeposition of bimetallic shells over Pd NCs was found to occur only for a lattice mismatch lower than 4.0%.[31] A higher lattice mismatch between the core and shell metals frequently results in the formation of core−shell NCs of nonuniform shapes.[32,33] However, some previous efforts report on the controlled disposition of Cu or AuCu on Pd nanocube seeds by tailoring the reduction kinetics in seed-mediated synthesis, which usually results in the formation of nonhomogeneous shell thickness or concave NCs.[28,29,34] For example, Meng et al.[34] demonstrated the deposition of AuCu on Pd nanocubes by combining sluggish reduction kinetics and lattice mismatch (∼4.02%), generating tetrapod-shaped Pd@AuCu core−shell NCs. A similar effort for covering Pd nanocubes by Cu (having lattice mismatch ∼7.1%) through the seed-mediated chemical reduction process resulted in the formation of branched Pd@Cu nanostructures. It is well known that the lattice mismatch between Pd and Cu is around 7.1%,[29] and the same for Pd and Au is about 4.8%.[35] Moreover, due to the high bonding energy of Au−Cu (235.6 kJ/mol),[36] their simultaneous deposition over Pd NCs in the seed-mediated growth process frequently occurs in island growth mode (Volmer−Weber mode),[28,37] generating final structures with concave surfaces. Therefore, uniform conformal deposition of bimetallic AuCu shells over Pd NCs with a predetermined final shape and controlled shell thickness remained a great challenge.[38]

Herein, we demonstrate a facile approach for the synthesis of multimetallic Pd@AuCu$_{nL}$ core−shell nanocubes with ultrathin AuCu bimetallic shells containing low Cu contents despite their large lattice mismatch. The AuCu alloy shells were conformally deposited onto Pd nanocube seeds through a kinetically controlled reduction and ligand-exchange reaction at room temperature. The obtained Pd@AuCu$_{nL}$ core−shell nanocubes have been tested as catalysts for the reduction of 4-nitrophenol by NaBH$_4$. The Pd@AuCu$_{6L}$ core−shell nanocubes were seen to exhibit remarkably high catalytic activity for 4-nitrophenol degradation by NaBH$_4$ relative to the Pd NCs and Pd@AuCu$_{12L}$ NCs.

2. EXPERIMENTAL SECTION

2.1. Chemicals and Materials. Sodium tetrachloropalladate(II) (Na$_2$PdCl$_4$, 99.99%), potassium bromide (KBr, 99%), gold(III) chloride tetrahydrate (HAuCl$_4$·4H$_2$O, 99.9%), copper chloride (CuCl$_2$, 99.99%), poly (vinyl pyrrolidone) (PVP, M_w 55 000), L-ascorbic acid (H$_2$Asc, 99%), sodium hydroxide (NaOH, 98%), and 4-nitrophenol were purchased from Sigma-Aldrich. All of the chemicals were used as received, without further purification. Deionized (DI) water from a Millipore system (resistivity >18.2 MΩ·cm) was utilized for the preparation of aqueous precursor solutions and sample washing.

2.2. Synthesis of Pd Nanocubes. The Pd nanocubes of ca. 13.5 nm average size were synthesized following the procedure we reported earlier.[4] In a typical synthesis, PVP (100 mg), L-ascorbic acid (60 mg), KBr (300 mg), and Na$_2$PdCl$_4$ (57 mg) were mixed in 15 mL of DI water in a glass beaker and heated for 3 h at 80 °C under continuous magnetic stirring. The reaction mixture was then cooled down to room temperature, and the product was separated by centrifugation (12 000 rpm for 10 min). Obtained Pd nanocubes were washed thoroughly by DI water and redispersed in DI water for characterization and further use.

2.3. Synthesis of Pd@AuCu$_{nL}$ Core−Shell Nanocrystals. In a typical synthesis process of Pd@AuCu$_{nL}$ core−shell NCs, 100 mg of AA and 66.6 mg of PVP were dissolved in 15 mL of DI water in a glass vial. Five milliliters of aqueous suspension of Pd nanocube seeds (1 mg/mL) was added to the earlier solution under magnetic stirring for 15 min. After that, 0.5 mL of aqueous NaOH (0.2 M) solution was added to adjust the pH of the reaction mixture to 11.5. Afterward, 0.1 mL (0.1 mM) of aqueous solution of HAuCl$_4$ and 0.025 mL of CuCl$_2$ (0.1 mM) precursor solution were mixed, then the solution mixture was titrated slowly at a rate of 1 mL/h into the earlier reaction solution, and the reaction was allowed to continue for another 30 min. Finally, the formed Pd@AuCu core−shell NCs were collected by centrifugation (12 000 rpm for 30 min) and washed twice with DI water. To fabricate the Pd@AuCu nanocrystals with different shell thicknesses, reactions were performed at the same experimental conditions, except only varying the amounts of HAuCl$_4$ and CuCl$_2$ solutions (0.1 mL + 0.025 mL and 0.2 mL + 0.05 mL). A reference Pd@Au$_{nL}$ core−shell sample was also prepared under similar experimental conditions without utilizing the CuCl$_2$ precursor.

2.4. Characterization of Nanocrystals. The morphology and size of the fabricated Pd nanocubes and Pd@AuCu$_{nL}$ core−shell NCs were analyzed by a JEOL JEM-1010 transmission electron microscope (TEM), operating at 80 kV. For TEM analysis, the colloidal samples were drop-cast on carbon-coated Ni grids and dried at room temperature. To study the fine structure and elemental distribution at the core−shell interface, the nanocrystals of core−shell configuration were analyzed by a JEOL JEM ARM 200F scanning transmission electron microscope (STEM) with high-angle annular dark-field (HAADF) imaging facility. The HAADF-STEM images of the samples were recorded at 200 kV operating voltage of the microscope. The elemental composition of the core−shell nanocubes was determined through energy-dispersive spectroscopy (EDS) inside TEM along with inductively coupled plasma (ICP) spectroscopy. For ICP analysis of the nanocrystals, about 1 mL of their colloidal solution of 1 mg/mL concentration was diluted with 40 mL of DI water prior to ICP analysis. The crystallinity and structural phase of the fabricated nanocrystals were analyzed further by recording their X-ray diffraction (XRD) patterns under Cu Kα excitation (λ = 1.5406 Å) by a Rigaku Ultima IV diffractometer in parallel-beam geometry in 15−80° 2θ range. Optical absorption spectra of the colloidal nanocrystals were recorded by an Agilent 8453 ultraviolet−visible (UV−vis) spectrophotometer in the 400−1100 nm spectral range. Geometric phase analysis (GPA) was performed using the FRWR tools plugin developed by Christoph T. Koch. Strain analysis was performed using the software based on the theory developed by Hÿtch et al.[39]

2.5. Catalytic Performance of Pd@AuCu$_{nL}$ Core−Shell Nanocubes in 4-Nitrophenol Degradation by NaBH$_4$. Reduction of 4-nitrophenol (4-NP) to 4-aminophenol (4-AP) by sodium borohydride (NaBH$_4$) was selected as a probe

reaction for testing the catalytic performance of the fabricated nanocrystals, especially to study the effect of AuCu alloy shells. Catalytic reduction of 4-nitrophenol (4-NP) by NaBH$_4$ was carried out in aqueous suspension at room temperature. For catalytic tests, first, we prepared aqueous colloidal solutions of all of the nanocrystals (Pd nanocubes, Pd@AuCu$_{6L}$, and Pd@AuCu$_{12L}$ core−shell NCs) maintaining a fixed (1 mg/mL) metal concentration in them. Separately, aqueous solutions of 4-NP were prepared by dissolving 5.56 mg of 4-NP in 200 mL of DI water to obtain the concentration of 0.2 mM. Then, 4 mL of this solution was mixed with 12 mL of DI water in a 20 mL vial. Then, 2 mL of this 4-NP solution was taken in a quartz cuvette, and 1 mL of NaBH$_4$ (10 mg/mL) solution was added. The color of the solution changed from light yellow to bright yellow immediately after the addition of freshly prepared NaBH$_4$ solution. After a few minutes of agitation, 25 μL of colloidal catalyst (Pd nanocubes, Pd@AuCu$_{6L}$, or Pd@AuCu$_{12L}$) was injected to the reaction mixture. The UV−vis absorption spectra of the reaction mixture were recorded at different time intervals (t = 0−20 min) in the 290−650 spectral ranges.

3. RESULTS AND DISCUSSION

A seed-mediated coreduction approach was adopted to achieve Pd@AuCu core−shell NCs with controlled AuCu shell thickness, as depicted in Scheme 1. First, the monodisperse

Scheme 1. Schematic Illustration Showing the Steps Involved in the Ligand-Exchange Synthesis of Multimetallic Pd@ AuCu$_{nL}$Core−Shell Nanocrystals
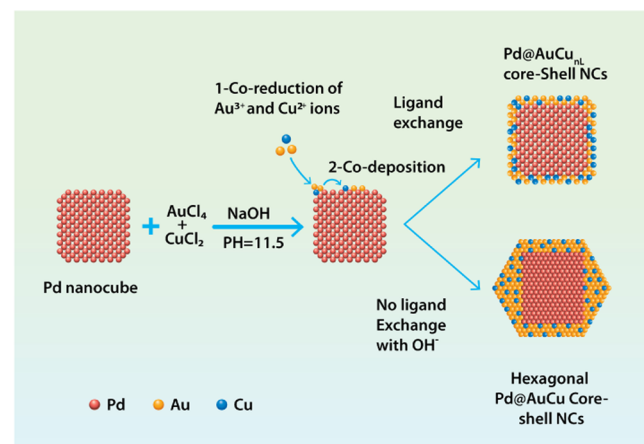
Pd Nanocube (NC) seeds of about 13.5 ± 2.5 nm average size were synthesized following the procedure we reported earlier (Figure S1, Supporting Information).[4] Then, AuCu alloy shells were deposited over the Pd nanocubes by controlled coreduction of Au and Cu metal ions with low Cu contents. To perform the latter step, presynthesized Pd NCs were dispersed in an aqueous solution containing ascorbic acid (H$_2$Asc, AA) and poly (vinyl pyrrolidone) (PVP) under magnetic stirring. The pH of the reaction mixture was adjusted to 11.5 by dropwise addition of aqueous NaOH solution. The basic reaction mixture was titrated at room temperature by slow addition of aqueous metal precursor solution (mixture of 0.1 M HAuCl$_4$ and 0.1 M CuCl$_2$ solutions in 4:1 v/v). A syringe pump was utilized to add the mixed metal precursor solution (see Section 2 for more details). Upon slow titration of HAuCl$_4$ and CuCl$_2$ in the presence of NaOH, two main

reactions took place: first, quick neutralization of H$_2$Asc by NaOH, resulting in the formation of H$_2$Asc$^-$. H$_2$Asc$^-$ exhibits higher reduction power than H$_2$Asc, which increases the reduction rate of the metal ions.[40] Second, the HAuCl$_4$ and CuCl$_2$ mixed precursor solution was quickly neutralized by NaOH to generate HAuCl$_4^-$ and CuCl$_2^-$ ions, followed by ligand exchange between the precursors and OH$^-$. The ligand exchange between HAuCl$_4^-$ and OH$^-$ lead to the conversion of HAuCl$_4^-$ into AuCl (OH)$_3^-$ and Au (OH)$_4^-$. Likewise, CuCl$_2^-$ converted to CuCl (OH)$^-$ and Cu(OH)$_2^-$.[41] These new products have relatively lower reduction potential in comparison to the reduction potentials of HAuCl$_4^-$ and CuCl$_2$.[41,42] Under a slow reduction rate, the reduction of these new products is dominated by H$_2$Asc$^-$, forming uniform conformal deposition of AuCu alloy layers onto the Pd NCs due to the OH$^-$ ion-mediated ligand-exchange effect.[42]

Scanning transmission electron microscopy (STEM) was utilized to characterize the as-prepared core−shell nanocubes. Figure 1a displays the typical high-angle annular dark-field
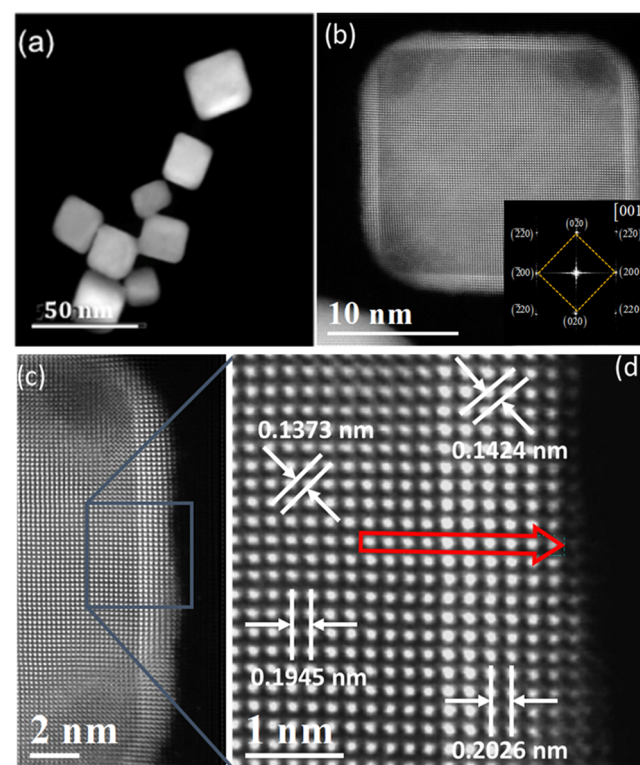
Figure 1. Structural and compositional analyses of the multimetallic Pd@AuCu$_{6L}$ core−shell NCs. (a) Typical low-magnification HAADF-STEM image, (b) high-resolution HAADF-STEM image of a Pd@AuCu$_{6L}$ core−shell nanocubes; inset: fast Fourier transform (FFT) pattern. (c) Section of the HAADF-STEM image of the particle shown in (b) and (d) amplified view of the elected region showing atomic stacking of Pd and AuCu. Formation of six atomic layers of AuCu shells over the Pd nanocube in most of the portion of its surface can be noticed in (d).

(HAADF)-STEM image of a representative Pd@AuCu core−shell nanocube sample, demonstrating the formation of core−shell NCs, preserving the initial cubic shape of seed Pd NCs in the final structures. Figure 1b,c shows high-resolution (HR) HAADF-STEM images of an individual Pd@AuCu$_{6L}$ core−shell nanocube, which revealed a sharp contrast difference between a well-crystalline Pd nanocube core and a AuCu shell

around it, clearly demonstrating the successful formation of core–shell NCs. As can be seen, the single crystalline Pd core is free from twins or grain boundaries as revealed by the homogeneous image contrast and long-range ordering of the particle. The observed contrast difference between the Pd core and AuCu shell is due to the difference in the average atomic number of individual atom columns. As the intensity of the HAADF-STEM images is almost proportional to the square of the atomic number (Z^2),[42] atomic columns with higher average atomic numbers exhibit higher intensity. For the same reason, the AuCu alloy shell shows a brighter contrast than the Pd core. Figure 1d depicts the HR-STEM image extracted from the region marked in Figure 1c, which shows the formation of a AuCu bimetallic shell of quite uniform thickness. As can be seen in Figure 1d, the bimetallic AuCu shell formed over the Pd NC consists of about six atomic layers. It should be noted that both Pd and AuCu alloy have face-center cubic (fcc) crystal lattice. From the HAADF-STEM image, d-spacings of 0.1945 and 0.1373 nm were estimated, which correspond to the {200} and {220} lattice planes of the Pd core, and the NC is oriented at the long [001] zone axis as shown in fast Fourier transform (FFT) pattern (inset of Figure 1b). The interplane distance of the {200} lattice planes demonstrates that the surfaces of fcc-structured Pd NCs have selectively exposed {100} surfaces. In addition, the Pd NCs have slightly truncated corners presenting {111} facets. The growth direction of the shell is guided by lattice matching along the six {100} and {111} surface planes of the Pd core. Therefore, the lattice planes of the shell layer also share the same orientation with Pd cores, with d-spacing values of 0.2026 and 0.1424 nm for the {200} and {220} lattice planes of the AuCu alloy structure, respectively. It should be mentioned that the observed d-spacing values in the AuCu shell layer are very close to the d-spacing values of the fcc Au lattice, indicating that the incorporated Cu atoms substitute Au atoms from its lattice, causing only a slight change in its interplanar distance or lattice constant.

Lattice strain in the Pd@AuCu core–shell NCs was determined using a geometric phase analysis (GPA) method. The GPA mapping analysis allows us to observe strained zones with varying degrees of atomic position displacement in the core–shell NCs with respect to an unstrained lattice.[43,44] Therefore, the GPA analysis was performed for Pd@AuCu$_{6L}$ core–shell NCs, as shown in the HAADF-STEM image presented in Figure S2 (Supporting Information). The Pd core and AuCu shell regions were selected for GPA, in which the core region of the image was used as the reference. As can be seen from Figure S2b (Supporting Information), the strain field is uniform in the core region. An expansive lattice deformation (orange color contrast) is present only in the shell layers. It is important to mention that the ε_{xy} and ε_{yy} strain fields only show the effect of the electron beam scans of the sample, and therefore, they are not shown. The ε_{xx} strain field map presented in Figure S2b shows the strain in the plane of the crystal face, which indicates an expansive deformation in the shell regions relative to the core regions. The expansive strain field in the shell region is due to the larger bulk lattice spacing of the AuCu alloy than the bulk latticing of Pd. The results obtained from GPA analysis suggest that the AuCu shell is undergoing slight expansive deformation due to lattice relaxation often observed when transitioning from the core–shell interface to the free surface.[44] In addition, the line profile across the NC further confirms that the relative deformation

near the AuCu shells is higher relative to the Pd core region in the Pd@AuCu$_{6L}$ core–shell NCs (Figure S2c, Supporting Information). These results suggest unambiguously that the slight expansive strains are present in the AuCu layers.

Slow injection of the mixed metal precursor (HAuCl$_4$ + CuCl$_2$) solution in the reaction mixture solution containing H$_2$Asc$^-$ and PVP causes the reduction of Au and Cu ions and subsequent deposition of Au and Cu atoms onto the Pd nanocube seeds through heterogeneous nucleation. Therefore, the thickness of the AuCu bimetallic shell over the Pd nanocube could be readily tuned by varying the amount of the precursor solution (HAuCl$_4$ and CuCl$_2$ mixture) in the reaction mixture. Figure 2 displays the typical HAADF-
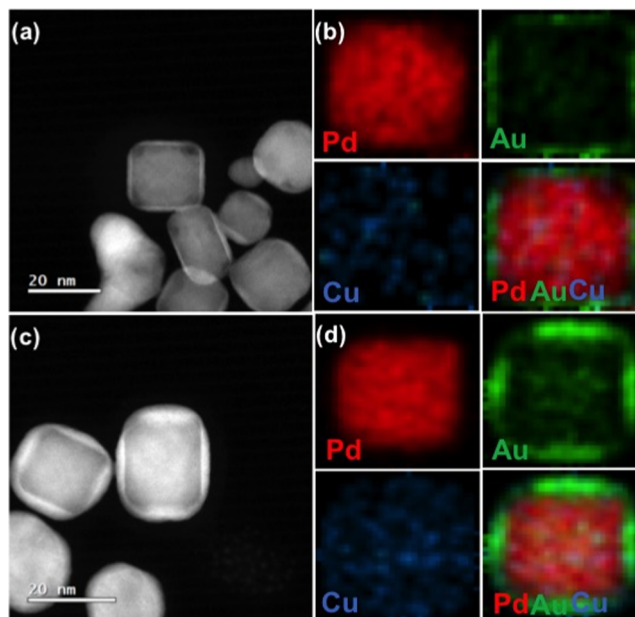

Figure 2. Controlling the number of AuCu atomic layers. (a, b) Typical HAAD-STEM image and EDX elemental mapping (in STEM) images of Pd@AuCu$_{6L}$ nanocubes. (c, d) Typical HAAD-STEM image and EDX elemental mapping (in STEM) images of Pd@AuCu$_{12L}$ core–shell nanocubes. Emission signals corresponding to Pd, Au, and Cu are presented in red, green, and blue, respectively.

STEM images and energy-dispersive X-ray spectroscopy (STEM-EDX) elemental mapping images of two different samples prepared by varying the amount of Au and Cu ion precursors, i.e., 0.1:0.025 and 0.2:0.05 mL (keeping the total ion concentration in the mixed precursor solution 0.1 mM) in the reaction mixture. As can be seen in Figure 2a,2c, core–shell nanocubes of different shell thicknesses were formed in the two cases. Formation of uniform AuCu bimetallic shells is quite evident in both samples. In addition, the EDX elemental mapping images of the samples in Figure 2b,d revealed that the signals of Pd and Au are located in the core and shell, while Cu exists both in core and shell regions, which is most likely due to the occurrence of Kirkendall effects between Pd and Cu.[45] Moreover, the EDX spectra of the Pd@AuCu core–shell nanocubes (Figure S3, Supporting Information) revealed the emission peaks of only Pd, Au, and Cu (apart from the Ni signal from the Ni grids utilized for TEM sample reparation) elements in them. Inductively coupled plasma atomic emission spectroscopy (ICP-AES) analysis was utilized to determine the Au/Cu ratio in the shell layers. The ICP-AES estimated that
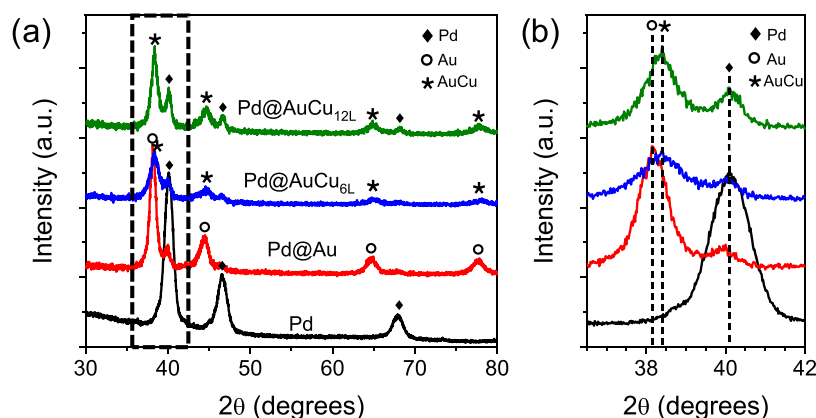
Figure 3. (a) XRD patterns of the Pd nanocubes and Pd@Au, Pd@AuCu$_{6L}$, and Pd@AuCu$_{12L}$ core−shell nanocrystals. (b) Magnified XRD spectra of the (111) diffraction peaks of corresponding samples.

Au/Cu ratio in the Pd@AuCu$_{6L}$ and Pd@AuCu$_{12L}$ samples were 7.45:1.87 and 15.3:3.9, respectively (Table S1, Supporting Information).

The structure of the samples was further analyzed by recording their X-ray diffraction (XRD) spectra. As can be seen in Figure 3a, all of the obtained Pd, Pd@Au, and Pd@AuCu$_{nL}$ NCs exhibited diffraction peaks of the face-center cubic (fcc) structure. The XRD pattern of Pd revealed the diffraction peaks at 2θ = 40.036, 46.712, and 68.256°, which are assigned to the (111), (200), and (220) planes of the fcc Pd, respectively (JCPDS No. 46-1043). For the sake of comparison, the XRD spectrum of Pd@Au core−shell NCs was included. The XRD pattern of Pd@Au revealed diffraction peaks of Pd in the fcc phase. Additional diffraction peaks appearing at 2θ = 38.159, 44.358, 64.67, and 77.664° could be indexed to the (111), (200), (220), and (311) crystalline planes of Au in the fcc phase, respectively (JCPDS No. 04-0784). The XRD patterns of Pd@AuCu$_{nL}$ revealed the diffraction peaks of fcc Pd, along with other diffraction peaks at 2θ = 38.437, 44.69, 65.02, and 78.27°, which are close to the diffraction peaks associated with Au appearing in the Pd@Au sample. However, the positions of these diffraction peaks were slightly shifted to higher diffraction angles compared to the pure fcc Au, indicating a slight decrease in lattice parameters due to the incorporation of Cu atoms in the Au lattice through substitution. Such a higher angle shift of the diffraction peaks can be ascribed to the formation of AuCu alloy shells on Pd NCs. The magnified region of (111) planes presented in Figure 3b showed a slight positive shift in the (111) peak position from 2θ = 36.5 to 42.0° relative to the Pd@Au NCs, suggesting that the AuCu shells are essentially in the alloy form, instead of the intermetallic phase.[34] The average crystallite size in the NCs was estimated from the Scherrer formula considering peak broadening.[46] Using the full width at half-maximum (FWHM) of (111) reflection, the obtained crystallite size of the Pd seed particles was 9 nm. In the case of Pd@AuCu$_{nL}$, as the most intense peaks of Pd and AuCu were overlapped, the peaks were deconvoluted to separate corresponding (111) reflections. The obtained average crystallite size values were 10 and 6 nm for the Pd and Pd@AuCu$_{6L}$ NCs and 10 and 9 nm for Pd and AuCu$_{12L}$ NCs, respectively.

It is well know that both Au and Cu exhibit localized surface plasmon resonance (LSPR) absorption peaks in the visible region. Therefore, we investigated the LSPR properties of the as-synthesized Pd nanocubes and Pd@Au, Pd@AuCu$_{6L}$, and Pd@AuCu$_{12L}$ core−shell nanocubes by UV−vis absorption spectroscopy (Figure S4, Supporting Information). As can be seen in Figure S4, the absorption spectrum of the colloidal Pd NCs is featureless, with absorption gradually increasing toward higher energy. On the other hand, the absorption spectrum of the colloidal Pd@Au core−shell NCs had a characteristic LSPR peak at around 526 nm, originating from the Au shell.[35] In the case of Pd@AuCu$_{6L}$ NCs, the LSPR peak was observed at 530 nm. As the thickness of the AuCu shell increased from 6 to 12 L, as expected, the position of the LSPR peak slightly red-shifted and the peak became slightly broadened, which is due to the incorporation of Cu in the Au layer of the Pd@AuCu core−shell NCs.[34] The Pd@AuCu$_{nL}$ core−shell NCs showed a slight broadening of the LSPR peak relative to Pd@Au NCs, which could be attributed to the involvement of quadrupolar and dipolar excitations.

A plausible reaction mechanism involved in the formation of atomically controlled AuCu shell layers over Pd NCs through conformal deposition of Au and Cu atoms can be described by the following steps: 1. Deposition of the reduced Au and Cu atoms initiate at the corner sites of the Pd nanocubes, i.e., over the {111} facets, as the side faces {100} remain covered with chemisorbed Cl$^-$ ions originating from the AuCl$_4^-$ and CuCl$_2^-$ precursors in the reaction solution. In the present synthesis, the conformal deposition of few atomic layers of AuCu shells onto Pd nanocubes was accomplished mainly through the combination of slow injection of the metal precursor (mixed precursor solution with low Cu content) and ligand exchange between the precursors and OH$^-$ ions. The ligand exchange between HAuCl$_4^-$ and CuCl$_2^-$ ions with OH$^-$ leads to the formation of AuCl(OH)$_3^-$, Au(OH)$_4^-$, and CuCl(OH)$^-$ and Cu(OH)$_2^-$, respectively. These newly generated products exhibit lower reduction potentials than their chloride counterparts. As a result, the Au and Cu ion precursors are reduced by HAsc$^-$ and Au and Cu atoms are epitaxially deposited over the Pd nanocubes. On the other hand, mixing metal ion precursors (CuCl$_2^-$ and HAuCl$_4^-$) at lower molar ratios (e.g., Au/Cu = 3:1) in the reaction solution weakens the lattice mismatch, favoring the formation of Pd@AuCu core−shell nanocubes. A similar phenomenon was documented by Meng et al.,[34] where the lattice mismatch was reduced by about 0.55% when AuCu was deposited onto Au$_3$Cu nanocube seeds.

To elucidate the growth mechanism, we performed several control experiments at different reaction conditions. In this
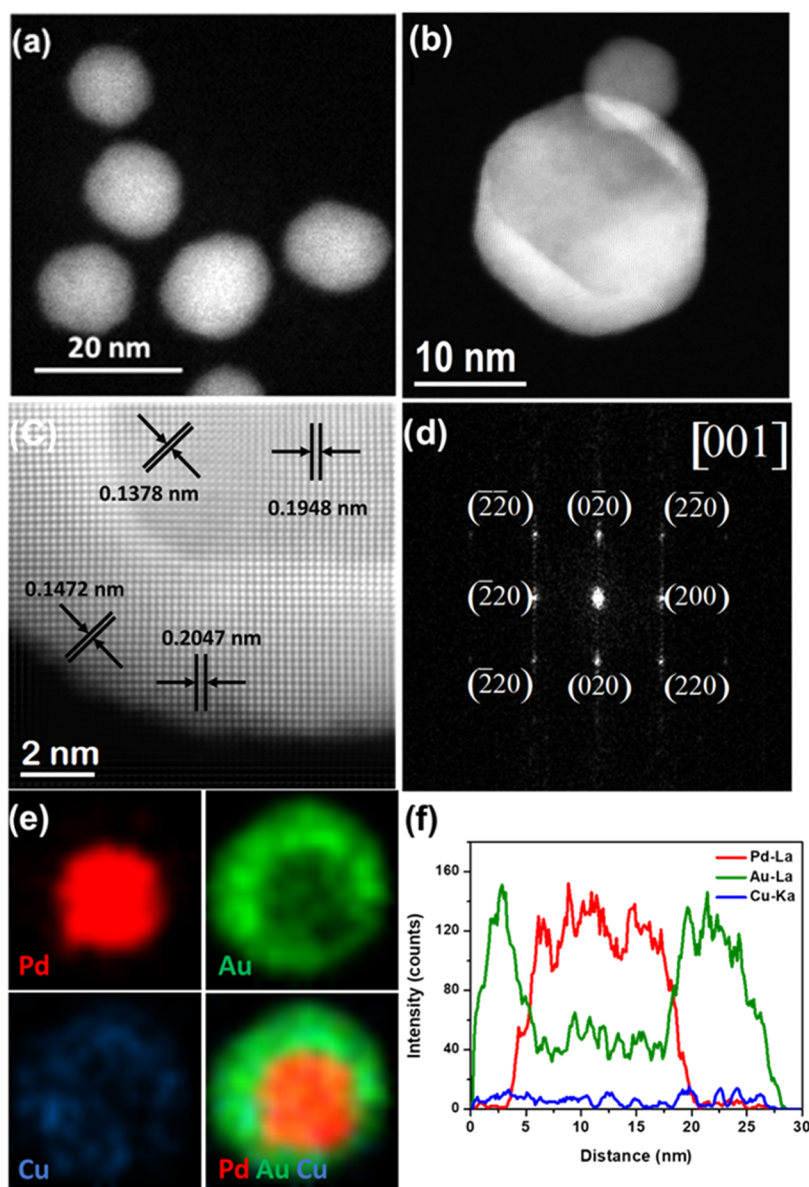
Figure 4. Structural characterization of the hexagonal Pd@AuCu core−shell NCs synthesized in the absence of NaOH in the reaction (pH 3.5). (a) HAADF-STEM image and (b) high-magnification STEM image of an individual NC, (c) atomic-resolution HAADF-STEM image taken from the corner region of the particle presented in (b), (d) FFT pattern extracted from the HAADF-STEM image presented in (c), (e) EDX elemental mapping images, and (f) EDX line-scan profiles of an individual hexagonal Pd@AuCu core−shell NC.

effort, we performed the synthesis by titrating 0.2 and 0.05 mL of the mixed Au and Cu metal ion precursor solutions in the aqueous colloidal solution of Pd NCs in the presence of AA and PVP, without introducing NaOH in the reaction. In the absence of NaOH, the pH of the reaction mixture was about 3.5. In this case, no neutralization and subsequent ligand-exchange process took place. Upon slow addition of the metal ion precursors in the reaction solution, the final products were hexagonal-shaped Pd@AuCu core−shell structures (Figure 4). As can be seen in the HAADF-STEM images (Figure 4a,b) of the product, the process produced nearly hexagonal Pd@AuCu core−shell NCs. The atomic-resolution HAADF-STEM image of the hexagonal NCs revealed the formation of about ten atomic layers of AuCu (Figure 4c). The crystallographic orientation of the NC was close to the [011] zone axis (Figure 4d). The obtained d-spacings of 0.2047 and 0.1472 nm corresponded to the {111} and {220} lattice planes of the

AuCu alloy structure, respectively. In addition, the measured d-spacings of 0.1948 and 0.137 8 nm corresponded well to the {200} and {220} lattice planes of the Pd core, respectively. Formation of the core−shell structure could be confirmed further by their EDX elemental mapping (Figure 4e) and line profile analysis (Figure 4f). EDX elemental mapping of the NCs clearly revealed the presence of Au and Cu in the shell and Pd in the core, indicating the formation of the Pd@AuCu core−shell configuration. On the other hand, the EDX line profile recorded over an individual (Figure 4f) NC revealed the formation of the core−shell structure, along with the spatial distribution of the elements across it.

As can be noticed, the concentration of the Cu element in the shell layer is substantially lower than that of the Au element, which is in accordance with the molar ratio of the elements used in the synthesis. The growth of hexagonal Pd@AuCu NCs instead of cubic shape could be attributed to the
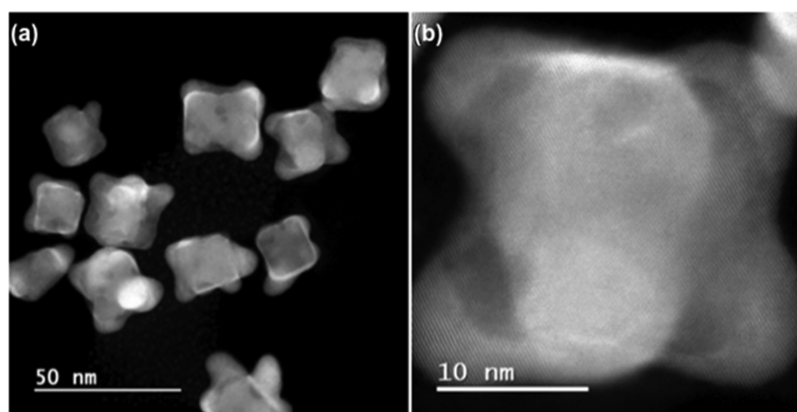
Figure 5. (a, b) Low- and high-magnification HAADF-STEM image of the concave-shaped Pd@AuCu core−shell nanocrystals synthesized through the standard procedure replacing L-AA with weak reducing agent D-glucose.
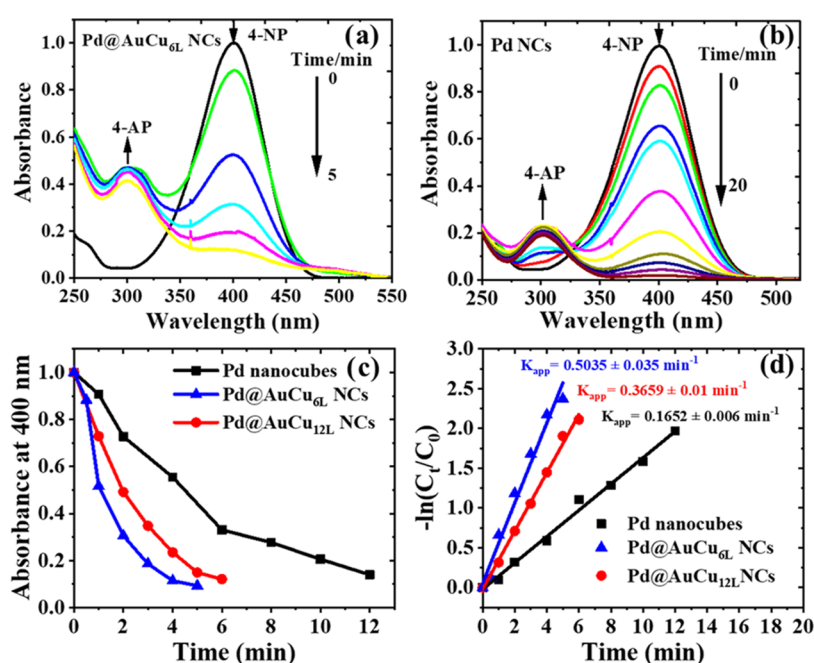

Figure 6. Comparison of the catalytic performance of Pd@AuCu$_{nL}$ core−shell NCs toward the reduction of 4-nitrophenol with NaBH$_4$. (a, b) Normalized UV−vis absorption spectra recorded at different reaction times for Pd@AuCu$_{6L}$ and Pd NCs; (c) comparison of the 400 nm absorption peak intensity with respect to its initial value during 4-NP reduction process; and (d) plots of $-\ln(C_t/C_0)$ versus time for the Pd NCs, Pd@AuCu$_{6L}$, and Pd@AuCu$_{12L}$ core−shell NC catalysts.

relatively lower deposition rates of Au and Cu atoms onto Pd NC seeds in the absence of OH$^-$ ion species in the reaction solution and hence the absence of the ligand-exchange process. Based on these results, it is evident that introduction of an adequate amount of NaOH is essential to induce the conformal deposition of AuCu shells on the surface of cubic Pd cores.

To verify the growth mechanism further, we repeated the same synthesis without adding Cu ion precursor in the reaction mixture, i.e., the epitaxial deposition of only Au layer over the Pd NCs at the same synthesis conditions utilized for Pd@AuCu NCs. In this process, we could epitaxially deposit Au shells of about six atomic layer thicknesses onto the Pd nanocubes (Figure S5, Supporting Information). The *d*-spacing values of 0.2038 and 0.1461 nm in the shell layer matching well with the *d*-spacing values of fcc Au lattice.[47] Utilization of same synthesis procedure to grow PtCu shells over Pd nanocubes resulted in the formation of Pd@PtCu$_{nL}$

core−shell NCs with slight strain at the interface (Figure S6, Supporting Information), which is attributed to the higher lattice mismatch between Pd core Cu (7.1%),[28] despite of both Pd and Pt have similar lattice mismatch. As can be noted in the EDX-mapping results presented in Figure S6, while the Pt signals exist only in the shell region, Cu signals appeared both in the core and shell regions, which can be attributed to the occurrence of galvanic replacement reactions.[45]

To further study the reduction kinetics, we performed synthesis replacing AA and NaOH by a weak reducing agent D-glucose, keeping all of the other conditions the same. The synthesis resulted in the formation of concave-edged Pd@AuCu NCs (Figure 5a,b). The result was primarily due to the week reducing power of D-glucose. Due to the slow reduction rate, the reduced Au and Cu atoms were deposited at the energetically favorable corner sites of Pd NCs, without diffusing to other faces of the Pd NCs. Similar tendency had also been observed in the earlier studies during the growth of

Table 1. Comparison of 4-NP Degradation Performance of the As-Synthesized Pd@AuCu$_{6L}$ Core−shell NC Catalyst with Previously Reported Mono/Bi- and Multimetallic Nanoparticle Catalysts

catalysts	size (nm)	4-NP concentration (mM)	NaBH$_4$ (mM)	K_{app} (min^{-1})	ref
Au nanoprisms	50.4 ± 11.4	675	0.27	0.36	60
Ru nanoframes	6.1	0.15	10	0.022	54
Au−Pd nanostars	62.8 ± 7.5	0.1	30	0.56	53
MCA Pd-Au(1:1)	3.5 ± 1.5	0.045	3.9	0.28	57
hollow Cu$_2$O-CuO/Au	25.0	0.06	5.0	0.43	61
Au@Cu core−shell nanocubes	77.9 ± 3.3	0.025	0.75	0.0722	58
Pd@Cu core−shell nanocubes	49 ± 1.5	0.025	0.75	0.02520	59
Au@CuPt core−shell NSs	9.1	1.0	100	0.05	56
Pd@AuCu$_{6L}$ NCs	13.5 ± 3.5	0.2	10	0.5035 ± 0.035	this work

Pd@AuCu tetrapods[34] and concave Pd@Pt core−shell NCs.[24] Formation of concave Pd@AuCu NCs was further confirmed by UV−vis analysis, which showed a new peak at 300 nm (Figure S7, Supporting Information) attributed to concave NCs.[34] The capping agent PVP also played a pivotal role in the conformal deposition of AuCu shells of uniform thickness onto Pd nanocube seeds. Specifically, PVP can be selectively bonded to the {100} facets of Pd nanocube seeds, facilitating the reduced Au and Cu adatoms to initially deposit on energetically favorable {110} facets (i.e., at the edges of the Pd nanocubes) and to diffuse into other faces latter on. Notably, in the absence of PVP in the reaction mixture, while keeping all of the other conditions the same, tiny bimetallic AuCu nanoparticles were deposited randomly on the surface of Pd nanocubes (Figure S8, Supporting Information), clearly indicating the important role of the capping agent in the epitaxial deposition process.

3.1. Catalytic Activity of Pd@AuCu$_{nL}$ Core−Shell NCs for 4-NP Degradation. Compared to the nonprecious metal catalysts, metallic or bimetallic NCs have shown to exhibit better catalytic performance.[48] In fact, the presence of bimetallic AuCu clusters over metal oxide nanoparticles has been seen to enhance their catalytic activity toward 4-NP reduction manifold in comparison to the composite nanostructures with single metal Au or Cu clusters.[38] Owing to the presence of multimetallic components in the Pd@AuCu core−shell NCs, exposed atomic arrangements, and synergetic effect of AuCu bimetallic shells over Pd nanocubes, they are expected to exhibit improved catalytic activity in a variety of chemical reactions.[15,49−51] To assess the potential catalytic performance of the as-synthesized Pd@AuCu$_{nL}$ NCs, their catalytic activities toward the reduction of 4-nitrophenol (4-NP) to 4-aminophenol (4-AP) by NaBH$_4$ were evaluated at room temperature as a model catalytic reaction. 4-NP exhibited its characteristic absorption band at 317 nm, which gets shifted to 400 nm after the addition of NaBH$_4$ due to the formation of 4-nitrophenolate ions (Figure S9, Supporting Information). The intensity of the 4-nitrophenolate ion absorption peak at 400 nm gradually decreased as the reduction reaction proceeded by the metal catalysts. Therefore, the reaction kinetics was monitored by UV−vis absorption spectroscopy. The intensity of 4-NP at 0 s was considered as the initial concentration before the addition of catalysts. Although the reduction of 4-NP by NaBH$_4$ was thermodynamically favored due to the positive difference between their standard electrode potentials $\left(\Delta E_0 = E_0(\text{4-NP/4-AP}) - E_0(\text{H}_3\text{BO}_3/\text{BH}_4^-) = 0.67 \text{ V}\right)$, it was kinetically restricted in the absence of a catalyst.[52] The reduction of 4-NPs to 4-AP is also possible without any

metallic catalysts; however, the reduction is extremely slow, typically exceeds 400 min.[53]

Figure 6a,b displays the UV−vis absorption spectra of the aliquots collected from the reaction mixture at different intervals after the addition of Pd@AuCu$_{6L}$ and Pd NC catalysts. As can be seen in Figure 6a,b after the introduction of catalysts, the intensity of the 4-nitrophenolate absorption peak at 400 nm gradually decreased, while an additional peak showed up at 315 nm for 4-AP. As can be seen in Figure 6a, for complete reduction of 4-NP to 4-AP, Pd@AuCu$_{6L}$ NC catalyst took less than 5 min, while the Pd@AuCu$_{12L}$ NC catalyst took about 6 min (Figurer S10, Supporting Information) and Pd NCs took more than 15 min (Figure 6b), confirming the superior catalytic activity of Pd@AuCu$_{6L}$ core−shell NCs. Figure 6c shows the absorption peak intensity at 400 nm as a function of reaction time (t) for the Pd@AuCu$_{6L}$ and Pd@AuCu$_{12L}$ core−shell NCs and Pd nanocubes. It is clear that the Pd@AuCu$_{6L}$ NCs catalyzed the reaction in a much faster rate in comparison to the Pd@AuCu$_{12L}$ NCs and Pd nanocubes under the same reaction conditions. The concentration of NaBH$_4$ in the reaction mixture was excess relative to that of 4-NP; hence, the concentration of NaBH$_4$ was considered to be constant throughout the reduction reaction period. Therefore, pseudo-first-order kinetics were utilized to evaluate the performance of the catalysts by estimating their apparent reaction rate constant (K_{app}) using the relation

$$\frac{dC_t}{dt} = -k_{app} C_t \tag{1}$$

where C_t is the concentration of 4-nitrophenol at time t and K_{app} is the first-order rate constant. Since the absorbance at time t is proportional to C_t, $-\ln C_t/C_o$ was plotted against time (t) to estimate the K_{app} value for the catalysts. Pseudo-first-order kinetics was considered for the catalytic reduction of dilute 4-NP solution.[54] The pseudo-first-order reaction kinetics was followed by estimating the apparent reaction rate constant K_{app} from the $-\ln(C_t/C_0)$ vs reaction time (t) plots. The value of apparent reaction constant K_{app} was estimated from the slope of the linear fitting curve in Figure 6d.

As shown in Figure 6d, the estimated value of K_{app} for the Pd@AuCu$_{6L}$ NC catalyst was about 0.5035 ± 0.035 min^{-1}, which is three times higher than the K_{app} value estimated for Pd NCs (0.1652 ± 0.006 min^{-1}) and about 1.5 times higher than that of Pd@AuCu$_{12L}$ NCs (0.3659 ± 0.01 min^{-1}). From the above results, it is clear that the Pd@AuCu$_{6L}$ NCs exhibit substantially higher catalytic activity when compared to Pd NCs. The catalytic performance of the Pd@AuCu$_{6L}$ catalysts was compared with the previously reported bi/multimetallic NCs of different shapes, and the results are summarized in

Table 1. As can see from Table 1, it is clear that that the Pd@AuCu$_{6L}$ NCs exhibited a far superior performance than that of the previously reported mono/bi- or multimetallic nanostructure-based catalysts. The obtained K_{app} values are much higher than the reported K_{app} values for 4-NP reduction by spherical monometallic Au and Cu NP[55,56] as well as bimetallic Au/Pt NP catalysts.[57] Furthermore, the Pd@AuCu$_{6L}$ NC catalysts displayed an almost 7.1 times higher K_{app} value than that of previously reported Au@Cu core−shell nanocubes[58] and a tenfold higher value than that of the Pd@Cu core−shell nanocubes.[59] These observations suggest that the Pd@AuCu$_{6L}$ core−shell NCs with exposed AuCu atomic layers enclosed by specific {100} and {111} faceted surfaces provide higher specific surface area and more active catalytic sites, which strengthens the absorption of the H$^{\bullet}$ species onto the surface, resulting in improved catalytic activity in comparison with spherical NPs.

It is well known that the catalytic reduction reaction of 4-NP on the metal NP surface is governed by the Langmuir−Hinshelwood mechanism.[62] The overall reaction occurs in three steps: (i) surface adsorption of 4-NP onto the catalyst surface, (ii) adsorption of active H$^{\bullet}$ radical species generated upon NaBH$_4$ reacting with H$_2$O, resulting in the formation of metal-H$^{\bullet}$ and subsequent conversion of 4-NP to 4-AP, and (iii) desorption of 4-NP molecules from the catalyst surface.[62,63] Therefore, competitive adsorption of both 4-NP and H$^{\bullet}$ species onto the same active sites of the catalyst surface and a follow-up interfacial charge transfer process involved in the reaction determined the rate of the reaction.[53] A significantly higher catalytic activity of the Pd@AuCu$_{6L}$ NCs might be due to the charge transfer between core and shell components, leading to a change in the charge density on the NC surface.[8] The presence of few atomic layered AuCu alloy shells over the Pd nanocubes creates charge heterogeneity on the surface of the catalyst. It should be noted that the work functions of Pd, Au, and Cu are about 5.6, 5.3, and 4.5 eV, respectively.[58,64] Due to the net differences in work function values, charge transfer occurs from Pd to Au and Cu surfaces.[64] Charge redistribution on the Pd@AuCu$_{nL}$ NC catalyst surface strengthens the adsorption of H$^{\bullet}$ radical species and the subsequent rate of reaction for 4-NP reduction. In addition, the slight compressive strain imposed on the AuCu shells can also contribute to enhancing the binding strength of H$^{\bullet}$ species on the catalyst surface, which can enhance the performance of the Pd@AuCu$_{nL}$ NC catalyst toward 4-NP reduction by NaBH$_4$. Thus, the combined action of cubic core−shell morphologies with exposed atomic arrangements, the charge redistribution between core−shell elements, and lattice-mismatch-induced strain imposed on the ultrathin AuCu layers makes the Pd@AuCu$_{6L}$ core−shell NCs excellent catalysts for 4-NP degradation by NaBH$_4$.

4. CONCLUSIONS

In summary, we have demonstrated a synthesis strategy to control the growth of Pd@AuCu$_{nL}$ core−shell NCs with different shell thicknesses despite their considerable lattice mismatch constraints and investigated their catalytic performance toward 4-NP reductions with NaBH$_4$. The key to success in the synthesis process is attributed to the combination of sluggish reduction kinetics and a ligand-exchange reaction in the presence of NaOH, H$_2$Asc, and PVP. The AuCu shell thickness could be easily controlled by adjusting the concentration of Au and Cu precursor ions in the reaction

mixture. In the absence of NaOH, the reaction mixture does not produce Pd@AuCu core−shell NCs; instead, hexagonal-shaped Pd@AuCu core−shell NCs are produced. The Pd@AuCu$_{6L}$ core−shell NCs exhibited the highest catalytic activity toward 4-NP with NaBH$_4$ in comparison to the bare Pd nanocubes and Pd@AuCu$_{12L}$ core−shell NCs mainly due to the synergetic effect of the Pd core and the ultrathin AuCu shell. This work may offer a general synthetic platform to rationally design and synthesize multimetallic core−shell NCs with ultrathin thicknesses and compositions for application in a variety of catalytic reactions.

■ ASSOCIATED CONTENT

ⓢ Supporting Information

The Supporting Information is available free of charge at https://pubs.acs.org/doi/10.1021/acs.jpcc.1c00646.

> TEM images of Pd nanocubes, GPA analysis, EDX elemental analysis, UV−vis absorption spectra of Pd@AuCu core−shell NCs, STEM images of Pd@PtCu core−shell NCs, and UV−vis spectra of 4-NP reduction by the Pd@AuCu$_{12L}$ core−shell catalyst (PDF)

■ AUTHOR INFORMATION

Corresponding Authors

Siva Kumar Krishnan − *Instituto de Física, Benemérita Universidad Autónoma de Puebla, Puebla 72570, Mexico;* ⓞ orcid.org/0000-0002-9672-9335; Email: sivakumar@ifuap.buap.mx

Umapada Pal − *Instituto de Física, Benemérita Universidad Autónoma de Puebla, Puebla 72570, Mexico;* ⓞ orcid.org/0000-0002-5665-106X; Email: upal@ifuap.buap.mx

Authors

Rodrigo Esparza − *Centro de Física Aplicada y Tecnología Avanzada, Universidad Nacional Autónoma de México, Santiago de Querétaro, Qro 76230, México*

Daniel Bahena Uribe − *Advanced Laboratory of Electron Nanoscopy, Mexico D.F. 07360, Mexico*

Sundeep Mukherjee − *Department of Materials Science and Engineering, University of North Texas, Denton, Texas 76203, United States;* ⓞ orcid.org/0000-0002-1954-0045

Complete contact information is available at:
https://pubs.acs.org/10.1021/acs.jpcc.1c00646

Notes

The authors declare no competing financial interest.

■ REFERENCES

(1) Kwon, T.; Jun, M.; Lee, K. Catalytic Nanoframes and Beyond. *Adv. Mater.* **2020**, *32*, No. 2001345.

(2) Aslam, U.; Chavez, S.; Linic, S. Controlling Energy Flow in Multimetallic Nanostructures for Plasmonic Catalysis. *Nat. Nanotechnol.* **2017**, *12*, 1000−1005.

(3) Jang, H.; Kim, Y.; Huh, H.; Min, D. Facile Synthesis and Intraparticle Self- Catalytic Oxidation of Dextran-Coated Hollow Au À Ag Nanoshell and Its Application for Chemo-Thermotherapy. *ACS Nano* **2014**, *8*, 467−475.

(4) Krishnan, S. K.; Prokhorov, E.; Bahena, D.; Esparza, R.; Meyyappan, M. Chitosan-Covered Pd@Pt Core−Shell Nanocubes for Direct Electron Transfer in Electrochemical Enzymatic Glucose Biosensor. *ACS Omega* **2017**, *2*, 1896−1904.

(5) Gilroy, K. D.; Ruditskiy, A.; Peng, H.; Qin, D.; Xia, Y. Bimetallic Nanocrystals: Syntheses, Properties, and Applications. *Chem. Rev.* **2016**, *116*, 10414−10472.

(6) Cui, C.; Gan, L.; Heggen, M.; Rudi, S.; Strasser, P. Compositional Segregation in Shaped Pt Alloy Nanoparticles and Their Structural Behaviour during Electrocatalysis. *Nat. Mater.* **2013**, *12*, 765−771.

(7) Zhang, X.; Han, S.; Zhu, B.; Zhang, G.; Li, X.; Gao, Y.; Wu, Z.; Yang, B.; Liu, Y.; Baaziz, W.; et al. Reversible Loss of Core−Shell Structure for Ni−Au Bimetallic Nanoparticles during CO2 Hydrogenation. *Nat. Catal.* **2020**, *3*, 411−417.

(8) Tedsree, K.; Li, T.; Jones, S.; Chan, C. W. A.; Yu, K. M. K.; Bagot, P. A. J.; Marquis, E. A.; Smith, G. D. W.; Tsang, S. C. E. Hydrogen Production from Formic Acid Decomposition at Room Temperature Using a Ag-Pd Core-Shell Nanocatalyst. *Nat. Nanotechnol.* **2011**, *6*, 302−307.

(9) Luo, M.; Guo, S. Strain-Controlled Electrocatalysis on Multimetallic Nanomaterials. *Nat. Rev. Mater.* **2017**, *2*, No. 17059.

(10) Sasaki, K.; Naohara, H.; Choi, Y.; Cai, Y.; Chen, W. F.; Liu, P.; Adzic, R. R. Highly Stable Pt Monolayer on PdAu Nanoparticle Electrocatalysts for the Oxygen Reduction Reaction. *Nat. Commun.* **2012**, *3*, No. 1115.

(11) Chen, G.; Xu, C.; Huang, X.; Ye, J.; Gu, L.; Li, G.; Tang, Z.; Wu, B.; Yang, H.; Zhao, Z.; et al. Interfacial Electronic Effects Control the Reaction Selectivity of Platinum Catalysts. *Nat. Mater.* **2016**, *15*, 564−569.

(12) Zhang, S.; Zhang, X.; Jiang, G.; Zhu, H.; Guo, S.; Su, D.; Lu, G.; Sun, S. Tuning Nanoparticle Structure and Surface Strain for Catalysis Optimization. *J. Am. Chem. Soc.* **2014**, *136*, 7734−7739.

(13) Bu, L.; Zhang, N.; Guo, S.; Zhang, X.; Li, J.; Yao, J.; Wu, T.; Lu, G.; Ma, J. Y.; Su, D.; et al. Biaxially Strained PtPb/Pt Core/Shell Nanoplate Boosts Oxygen Reduction Catalysis. *Science.* **2016**, *354*, 1410−1414.

(14) Wang, C.; Sang, X.; Gamler, J. T. L.; Chen, D. P.; Unocic, R. R.; Skrabalak, S. E. Facet-Dependent Deposition of Highly Strained Alloyed Shells on Intermetallic Nanoparticles for Enhanced Electrocatalysis. *Nano Lett.* **2017**, *17*, 5526−5532.

(15) Yin, J.; Shan, S.; Yang, L.; Mott, D.; Malis, O.; Petkov, V.; Cai, F.; Shan Ng, M.; Luo, J.; Chen, B. H.; et al. Gold-Copper Nanoparticles: Nanostructural Evolution and Bifunctional Catalytic Sites. *Chem. Mater.* **2012**, *24*, 4662−4674.

(16) Hsu, S.-C.; Chuang, Y.-C.; Sneed, B. T.; Cullen, D. A.; Chiu, T.-W.; Kuo, C.-H. Turning the Halide Switch in the Synthesis of Au-Pd Alloy and Core-Shell Nanoicosahedra with Terraced Shells: Performance in Electrochemical and Plasmon-Enhanced Catalysis. *Nano Lett.* **2016**, *16*, 5514−5520.

(17) Zhong, J. H.; Jin, X.; Meng, L.; Wang, X.; Su, H. S.; Yang, Z. L.; Williams, C. T.; Ren, B. Probing the Electronic and Catalytic Properties of a Bimetallic Surface with 3nm Resolution. *Nat. Nanotechnol.* **2017**, *12*, 132−136.

(18) Bai, S.; Shao, Q.; Wang, P.; Dai, Q.; Wang, X.; Huang, X. Highly Active and Selective Hydrogenation of CO$_2$ to Ethanol by Ordered Pd−Cu Nanoparticles". *J. Am. Chem. Soc.* **2017**, *140*, 6827−6830.

(19) Sun, L.; Zhang, Q.; Li, G. G.; Villarreal, E.; Fu, X.; Wang, H. Multifaceted Gold-Palladium Bimetallic Nanorods and Their Geometric, Compositional, and Catalytic Tunabilities. *ACS Nano* **2017**, *11*, 3213−3228.

(20) Kim, J. S.; Kim, H. K.; Kim, S. H.; Kim, I.; Yu, T.; Han, G. H.; Lee, K. Y.; Lee, J. C.; Ahn, J. P. Catalytically Active Au Layers Grown on Pd Nanoparticles for Direct Synthesis of H$_2$O$_2$: Lattice Strain and Charge-Transfer Perspective Analyses. *ACS Nano* **2019**, *13*, 4761−4770.

(21) Xia, Y.; Gilroy, K. D.; Peng, H.-C.; Xia, X. Seed-Mediated Growth of Colloidal Metal Nanocrystals. *Angew. Chem., Int. Ed.* **2016**, *55*, 60−95.

(22) Weiner, R. G.; Kunz, M. R.; Skrabalak, S. E. Seeding a New Kind of Garden: Synthesis of Architecturally Defined Multimetallic Nanostructures by Seed-Mediated Co-Reduction. *Acc. Chem. Res.* **2015**, *48*, 2688−2695.

(23) Weiner, R. G.; Skrabalak, S. E. Seed-Mediated Co-Reduction as a Route to Shape-Controlled Trimetallic Nanocrystals. *Chem. Mater.* **2016**, *28*, 4139−4142.

(24) Xie, S.; Choi, S.; Lu, N.; Roling, L.; Herron, J.; Zhang, L.; Wang, J.; Kim, M. J.; Xie, Z.; et al. Atomic Layer-by-Layer Deposition of Pt on Pd Nanocubes for Catalysts with Enhanced Activity and Durability toward Oxygen Reduction. *Nano Lett.* **2014**, *14*, 3570−3576.

(25) Yang, T. H.; Gilroy, K. D.; Xia, Y. Reduction Rate as a Quantitative Knob for Achieving Deterministic Synthesis of Colloidal Metal Nanocrystals. *Chem. Sci.* **2017**, *8*, 6730−6749.

(26) Gilroy, K. D.; Yang, X.; Xie, S.; Zhao, M.; Qin, D.; Xia, Y. Shape-Controlled Synthesis of Colloidal Metal Nanocrystals by Replicating the Surface Atomic Structure on the Seed. *Adv. Mater.* **2018**, *30*, No. 1706312.

(27) Smith, J. D.; Scanlan, M. M.; Chen, A. N.; Ashberry, H. M.; Skrabalak, S. E. Kinetically Controlled Sequential Seeded Growth: A General Route to Crystals with Different Hierarchies. *ACS Nano* **2020**, *14*, 15953−15961.

(28) Jin, M.; Zhang, H.; Wang, J.; Zhong, X.; Lu, N.; Li, Z.; Xie, Z.; Kim, M. J.; Xia, Y. Copper Can Still Be Epitaxially Deposited on Palladium Nanocrystals to Generate Core-Shell Nanocubes despite Their Large Lattice Mismatch. *ACS Nano* **2012**, *6*, 2566−2573.

(29) Kunz, M. R.; McClain, S. M.; Chen, D. P.; Koczkur, K. M.; Weiner, R. G.; Skrabalak, S. E. Seed-Mediated Co-Reduction in a Large Lattice Mismatch System: Synthesis of Pd-Cu Nanostructures. *Nanoscale* **2017**, *9*, 7570−7576.

(30) Zhu, C.; Zeng, J.; Tao, J.; Johnson, M. C.; Schmidt-Krey, I.; Blubaugh, L.; Zhu, Y.; Gu, Z.; Xia, Y. Kinetically Controlled Overgrowth of Ag or Au on Pd Nanocrystal Seeds: From Hybrid Dimers to Nonconcentric and Concentric Bimetallic Nanocrystals. *J. Am. Chem. Soc.* **2012**, *134*, 15822−15831.

(31) Zhang, J.; Tang, Y.; Lee, K.; Ouyang, M. Nonepitaxial Growth of Hybrid Core-Shell Nanostructures with Large Lattice Mismatches. *Science.* **2010**, *327*, 1634−1639.

(32) Habas, S. E.; Lee, H.; Radmilovic, V.; Somorjai, G. A.; Yang, P. Shaping Binary Metal Nanocrystals through Epitaxial Seeded Growth. *Nat. Mater.* **2007**, *6*, 692−697.

(33) Desantis, C. J.; Skrabalak, S. E. Core Values: Elucidating the Role of Seed Structure in the Synthesis of Symmetrically Branched Nanocrystals. *J. Am. Chem. Soc.* **2013**, *135*, 10−13.

(34) Meng, M.; Fang, Z.; Zhang, C.; Su, H.; He, R.; Zhang, R.; Li, H.; Li, Z. Y.; Wu, X.; Ma, C.; et al. Integration of Kinetic Control and Lattice Mismatch to Synthesize Pd@AuCu Core-Shell Planar Tetrapods with Size-Dependent Optical Properties. *Nano Lett.* **2016**, *16*, 3036−3041.

(35) Lim, B.; Kobayashi, H.; Yu, T.; Wang, J.; Kim, M. J.; Li, Z.; Rycenga, M.; Xia, Y. Synthesis of Pd-Au Bimetallic Nanocrystals via Controlled Overgrowth Byungkwon. *J. Am. Chem. Soc.* **2010**, *132*, 2506−2507.

(36) Tsuji, M.; Yamaguchi, D.; Matsunaga, M.; Alam, M. J. Epitaxial Growth of Au@Cu Core-Shell Nanocrystals Prepared Using the PVP-Assisted Polyol Reduction Method. *Cryst. Growth Des.* **2010**, *10*, 5129−5135.

(37) Fan, F.; Liu, D.; Wu, Y.; Duan, S.; Xie, Z.; Jiang, Z.; et al. Epitaxial Growth of Heterogeneous Metal Nanocrystals: From Gold Nano-Octahedra to Palladium and Silver Nanocubes. *J. Am. Chem. Soc.* **2008**, 6949−6951.

(38) Alvarez-paneque, A. F.; Rodr, B.; Pastoriza-santos, I.; Liz-marzan, L. M. Shape-Templated Growth of Au @ Cu Nanoparticles. *J. Phys. Chem. C* **2013**, *117*, 2474−2479.

(39) Hÿtch, M. J.; Snoeck, E.; Kilaas, R. Quantitative Measurement of Displacement and Strain Fields from HREM Micrographs. *Ultramicroscopy* **1998**, *74*, 131−146.

(40) Sun, X.; Yang, Y.; Zhang, Z.; Qin, D. Mechanistic Roles of Hydroxide in Controlling the Deposition of Gold on Colloidal Silver Nanocrystals. *Chem. Mater.* **2017**, *29*, 4014−4021.

(41) Ahn, J.; Wang, D.; Ding, Y.; Zhang, J.; Qin, D. Site-Selective Carving and Co-Deposition: Transformation of Ag Nanocubes into Concave Nanocrystals Encased by Au-Ag Alloy Frames. *ACS Nano* **2018**, *12*, 298−307.

(42) Daniel, J. R.; McCarthy, L. A.; Yazdi, S.; Chagnot, M.; Ringe, E.; Boudreau, D. Gold Speciation and Co-Reduction Control the Morphology of AgAu Nanoshells in Formaldehyde-Assisted Galvanic Replacement. *J. Phys. Chem. C* **2018**, *122*, 18168−18176.

(43) Ramamoorthy, R. K.; Viola, A.; Grindi, B.; Peron, J.; Gatel, C.; Hytch, M.; Arenal, R.; Sicard, L.; Giraud, M.; Piquemal, J. Y.; et al. One-Pot Seed-Mediated Growth of Co Nanoparticles by the Polyol Process: Unraveling the Heterogeneous Nucleation. *Nano Lett.* **2019**, *19*, 9160−9169.

(44) Gamler, J. T. L.; Leonardi, A.; Sang, X.; Koczkur, K. M.; Unocic, R. R.; Engel, M.; Skrabalak, S. E. Effect of Lattice Mismatch and Shell Thickness on Strain in Core@shell Nanocrystals. *Nanoscale Adv.* **2020**, *2*, 1105−1114.

(45) Bao, M.; Amiinu, I. S.; Peng, T.; Li, W.; Liu, S.; Wang, Z.; Pu, Z.; He, D.; Xiong, Y.; Mu, S. Surface Evolution of PtCu Alloy Shell over Pd Nanocrystals Leads to Superior Hydrogen Evolution and Oxygen Reduction Reactions. *ACS Energy Lett.* **2018**, *3*, 940−945.

(46) Cullity, B. D. *Elements of X-Ray Diffraction*; Addison-Wesley Publishing, 1956; pp 1−509.

(47) Yuan, X.; Zhang, L.; Li, L.; Dong, H.; Chen, S.; Zhu, W.; Hu, C.; Deng, W.; Zhao, Z. J.; Gong, J. Ultrathin Pd-Au Shells with Controllable Alloying Degree on Pd Nanocubes toward Carbon Dioxide Reduction. *J. Am. Chem. Soc.* **2019**, *141*, 4791−4794.

(48) Formenti, D.; Ferretti, F.; Scharnagl, F. K.; Beller, M. Reduction of Nitro Compounds Using 3d-Non-Noble Metal Catalysts. *Chem. Rev.* **2019**, *119*, 2611−2680.

(49) Hajfathalian, M.; Gilroy, K. D.; Yaghoubzade, A.; Sundar, A.; Tan, T.; Hughes, R. A.; Neretina, S. Photocatalytic Enhancements to the Reduction of 4-Nitrophenol by Resonantly Excited Triangular Gold-Copper Nanostructures. *J. Phys. Chem. C* **2015**, *119*, 17308−17315.

(50) Zhu, W.; Zhang, L.; Yang, P.; Hu, C.; Dong, H.; Zhao, Z.-J.; Mu, R.; Gong, J. Formation of Enriched Vacancies for Enhanced CO_2 Electrocatalytic Reduction over AuCu Alloys. *ACS Energy Lett.* **2018**, *3*, 2144−2149.

(51) Zhan, W.; Wang, J.; Wang, H.; Zhang, J.; Liu, X.; Zhang, P.; Chi, M.; Guo, Y.; Guo, Y.; Lu, G.; et al. Crystal Structural Effect of AuCu Alloy Nanoparticles on Catalytic CO Oxidation. *J. Am. Chem. Soc.* **2017**, *139*, 8846−8854.

(52) Baruah, B.; Gabriel, G. J.; Akbashev, M. J.; Booher, M. E. Facile Synthesis of Silver Nanoparticles Stabilized by Cationic Polynorbornenes and Their Catalytic Activity in 4-Nitrophenol Reduction. *Langmuir* **2013**, *29*, 4225−4234.

(53) Ma, T.; Liang, F. Au-Pd Nanostars with Low Pd Content: Controllable Preparation and Remarkable Performance in Catalysis. *J. Phys. Chem. C* **2020**, *124*, 7812−7822.

(54) Ye, H.; Wang, Q.; Catalano, M.; Lu, N.; Vermeylen, J.; Kim, M. J.; Liu, Y.; Sun, Y.; Xia, X. Ru Nanoframes with an Fcc Structure and Enhanced Catalytic Properties. *Nano Lett.* **2016**, *16*, 2812−2817.

(55) Xu, P.; Cen, C.; Zheng, M.; Wang, Y.; Wu, Z.; Teng, Z. A Facile Electrostatic Droplets Assisted Synthesis of Copper Nanoparticles Embedded Magnetic Carbon Microspheres for Highly Effective Catalytic Reduction of 4-Nitrophenol and Rhodamine B. *Mater. Chem. Phys.* **2020**, *253*, No. 123444.

(56) Mehmood, S.; Janjua, N. K.; Saira, F.; Fenniri, H. AuCu@Pt Nanoalloys for Catalytic Application in Reduction of 4-Nitrophenol. *J. Spectrosc.* **2016**, *2016*, 1−8.

(57) Jiang, F.; Li, R.; Cai, J.; Xu, W.; Cao, A.; Chen, D.; Zhang, X.; Wang, C.; Shu, C. Ultrasmall Pd/Au Bimetallic Nanocrystals Embedded in Hydrogen-Bonded Supramolecular Structures: Facile Synthesis and Catalytic Activities in the Reduction of 4-Nitrophenol. *J. Mater. Chem. A* **2015**, *3*, 19433−19438.

(58) Hsia, C. F.; Madasu, M.; Huang, M. H. Aqueous Phase Synthesis of Au-Cu Core-Shell Nanocubes and Octahedra with Tunable Sizes and Noncentrally Located Cores. *Chem. Mater.* **2016**, *28*, 3073−3079.

(59) Zhang, G.; Feng, J.; Wang, S.; Xu, B.; Ding, W.; Wang, W.; Fu, Z. Stable Pd@Cu Core-Shell Nanocubes with Finely Tuned Sizes for the Reduction of Nitroaromatics. *ACS Appl. Nano Mater.* **2019**, *2*, 4584−4593.

(60) Park, S. I.; Song, H. M. Synthesis of Prolate-Shaped Au Nanoparticles and Au Nanoprisms and Study of Catalytic Reduction Reactions of 4-Nitrophenol. *ACS Omega* **2019**, *4*, 7874−7883.

(61) Yao, W.; Li, F.-L.; Li, H.-X.; Lang, J.-P. Fabrication of Hollow $Cu_2O@CuO$-Supported Au-Pd Alloy Nanoparticles with High Catalytic Activity through the Galvanic Replacement Reaction Wang. *J. Mater. Chem. A* **2015**, *3*, 4578−4585.

(62) Aditya, T.; Pal, A.; Pal, T. Nitroarene Reduction: A Trusted Model Reaction to Test Nanoparticle Catalysts. *Chem. Commun.* **2015**, *51*, 9410−9431.

(63) Strachan, J.; Barnett, C.; Masters, A. F.; Maschmeyer, T. 4-Nitrophenol Reduction: Probing the Putative Mechanism of the Model Reaction. *ACS Catal.* **2020**, *10*, 5516−5521.

(64) Sarina, S.; Bai, S.; Huang, Y.; Chen, C.; Jia, J.; Jaatinen, E.; Ayoko, G. A.; Bao, Z.; Zhu, H. Visible Light Enhanced Oxidant Free Dehydrogenation of Aromatic Alcohols Using Au-Pd Alloy Nanoparticle Catalysts. *Green Chem.* **2014**, *16*, 331−341.